High Photoluminescence Quantum Yield in Band Gap Tunable Bromide Containing Mixed Halide Perovskites

Carolin M. Sutter-Fella,[†,‡] Yanbo Li,[§,||] Matin Amani,[†,‡] Joel W. Ager, III,[‡,⊥] Francesca M. Toma,[§,||] Eli Yablonovitch,[†,‡] Ian D. Sharp,*[§,||] and Ali Javey*[†,‡]

[†]Electrical Engineering and Computer Sciences, University of California, Berkeley, California 94720, United States
[‡]Materials Sciences Division, [§]Joint Center for Artificial Photosynthesis, and [||]Chemical Sciences Division, Lawrence Berkeley National Laboratory, Berkeley, California 94720, United States
[⊥]Materials Science and Engineering, University of California, Berkeley, California 94720, United States

S Supporting Information

ABSTRACT: Hybrid organic−inorganic halide perovskite based semiconductor materials are attractive for use in a wide range of optoelectronic devices because they combine the advantages of suitable optoelectronic attributes and simultaneously low-cost solution processability. Here, we present a two-step low-pressure vapor-assisted solution process to grow high quality homogeneous $CH_3NH_3PbI_{3-x}Br_x$ perovskite films over the full band gap range of 1.6−2.3 eV. Photoluminescence light-in versus light-out characterization techniques are used to provide new insights into the optoelectronic properties of Br-containing hybrid organic−inorganic perovskites as a function of optical carrier injection by employing pumppowers over a 6 orders of magnitude dynamic range. The internal luminescence quantum yield of wide band gap perovskites reaches impressive values up to 30%. This high quantum yield translates into substantial quasi-Fermi level splitting and high "luminescence or optically implied" open-circuit voltage. Most importantly, both attributes, high internal quantum yield and high optically implied open-circuit voltage, are demonstrated over the entire band gap range (1.6 eV $\leq E_g \leq$ 2.3 eV). These results establish the versatility of Br-containing perovskite semiconductors for a variety of applications and especially for the use as high-quality top cell in tandem photovoltaic devices in combination with industry dominant Si bottom cells.

KEYWORDS: Halide perovskite, wide band gap semiconductor, quantum yield, tandem device
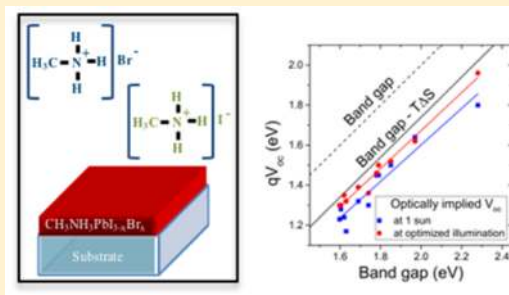
Hybrid organic−inorganic halide perovskites are a new class of semiconductors that have attracted significant research attention in the past few years.[1] These materials offer several advantages over conventional semiconductors such as low-cost solution processability[2,3] at low temperatures,[4] high defect tolerance,[5,6] and the tunability of the optical band gap over a large range.[7] Within this class of materials, methylammonium lead halides, $CH_3NH_3PbX_3$ (X = Cl, Br, I or combinations thereof) have been most extensively studied. Indeed, mixed I/Br halide perovskites ($CH_3NH_3PbI_{3-x}Br_x$) offer tunable band gaps in the visible and near-infrared range, from 1.57−2.29 eV.[7] Considering the facile methods used to deposit organic−inorganic perovskites, they possess surprisingly good optoelectronic attributes. These include high absorption coefficient,[8] low Urbach energy,[8] long minority carrier lifetime and diffusion lengths,[9−12] and high-photoluminescence quantum yield.[13,14] As a result, perovskites are not only attractive for the use in single junction solar cells, which have been demonstrated with certified efficiencies above 20%,[15,16] but are also promising candidates for application as the top cell in tandem devices, for example, in combination with Si[17−19] or Cu(In,Ga)Se$_2$.[19,20] Moreover, they offer

desirable properties for use as light-emitting devices such as LEDs[21,22] and lasers gain media.[13,23]

Specifically, for the case of tandem photovoltaic devices with a Si bottom cell (E_g = 1.12 eV), ideally a top cell with a band gap of ∼1.65−1.9 eV should be employed to reach efficiencies close to ∼40% under 1-sun AM1.5G illumination.[24,25] So far, the material choice for the top cell was limited to InGaP,[25] AlGaAs,[26] or (In)GaN.[27,28] There are, however, practical constraints related to growth of these semiconductors on Si, arising from large lattice mismatch and high-temperature processing requirements. Here, we show that mixed halide perovskites in the $CH_3NH_3PbI_{3-x}Br_x$ composition space combine low-temperature processability and high intrinsic material quality over the full band gap range from 1.6−2.3 eV, thus making them ideal candidates for tandem photovoltaic devices in combination with Si.

A universal metric to judge the intrinsic optoelectronic quality of a semiconductor is the internal radiative efficiency or
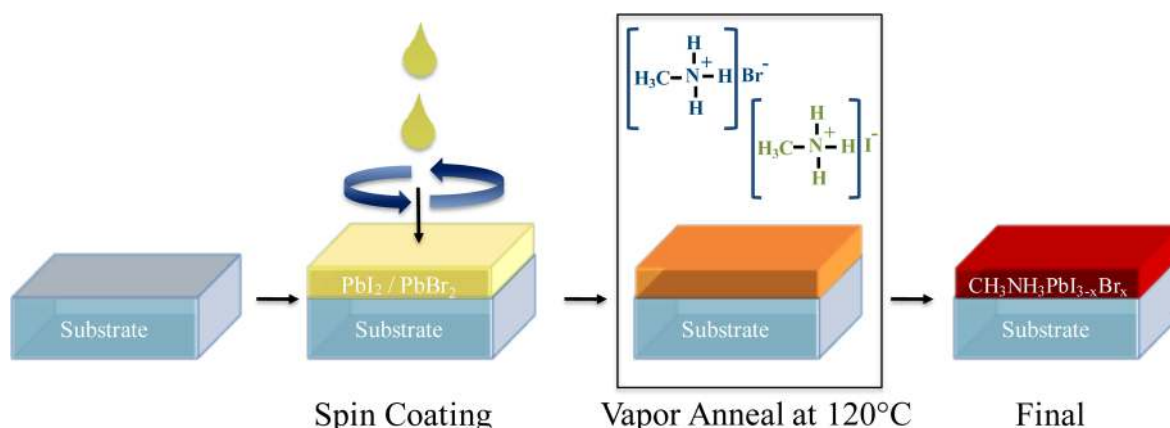
Figure 1. Process scheme for the low-pressure vapor-assisted solution process (LP-VASP). Mixed lead halide $PbI_2/PbBr_2$ is spin-coated onto the glass substrate, dried, and then annealed in CH_3NH_3I/CH_3NH_3Br vapor at low pressure to yield the $CH_3NH_3PbI_{3-x}Br_x$ films.
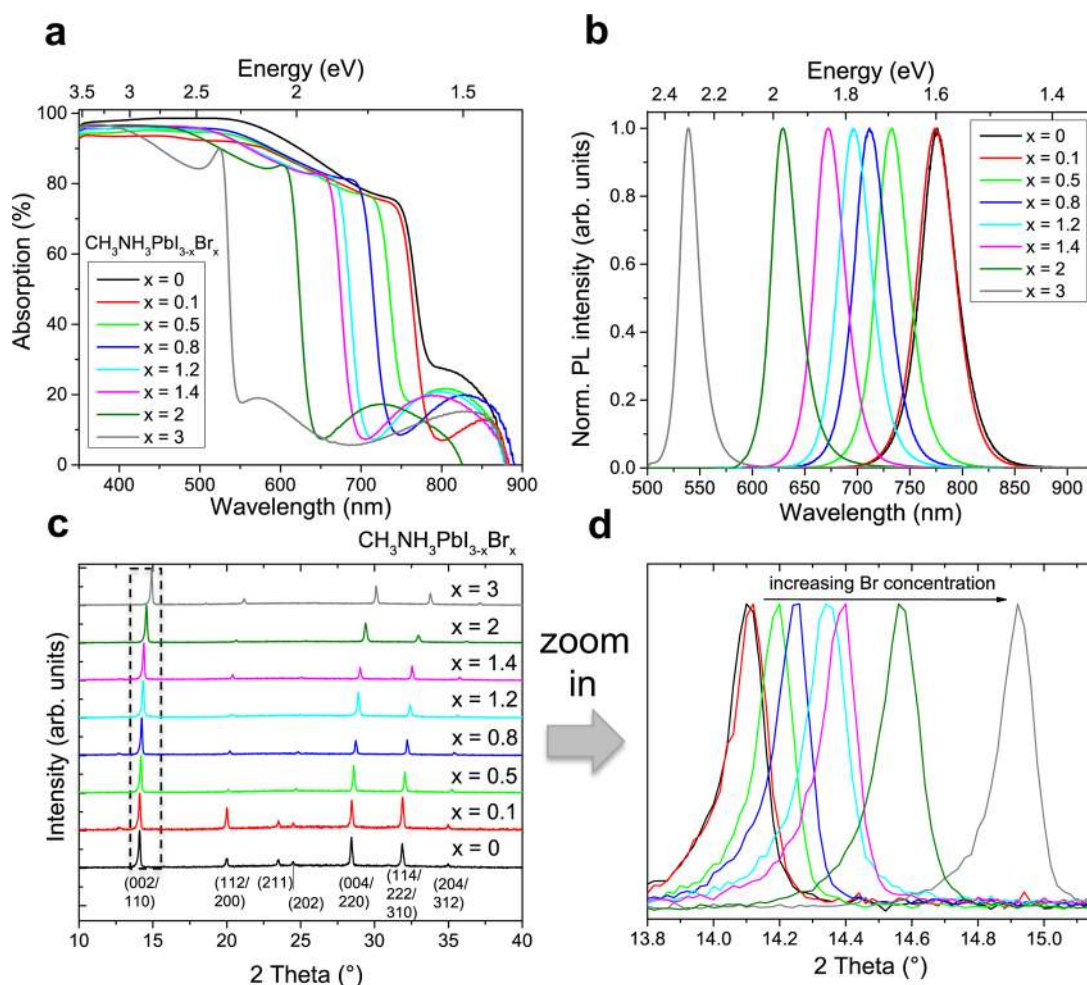
Figure 2. Br-containing perovskite film characterization. (a) UV−vis absorption spectra of perovskite films on glass substrate with PMMA cap extracted from transmittance and reflectance measurements. The below band gap absorption artifact seen for all samples is caused by constructive thin-film interference effects due to multiple reflections at the air/PMMA and PMMA/perovskite interfaces. (b) Photoluminescence spectra recorded at room temperature, excited with an argon laser (with λ = 514 nm; and for x = 3 with λ = 488 nm) and (c,d) X-ray diffraction patterns of the investigated set of samples.

internal photoluminescence (PL) quantum yield (iQY), which is defined as the number of photons radiatively emitted divided by the number of photons absorbed and corrected for the refractive index. This quantity is equivalent to the radiative recombination rate over the sum of radiative and nonradiative

recombination rates. In an ideal semiconductor material, there is only radiative recombination due to the absence of trap states, thus the iQY is 100%. Defects in the semiconductor, as well as at its interface, lead to nonradiative recombination at trap sites, also known as Shockley−Read−Hall (SRH)
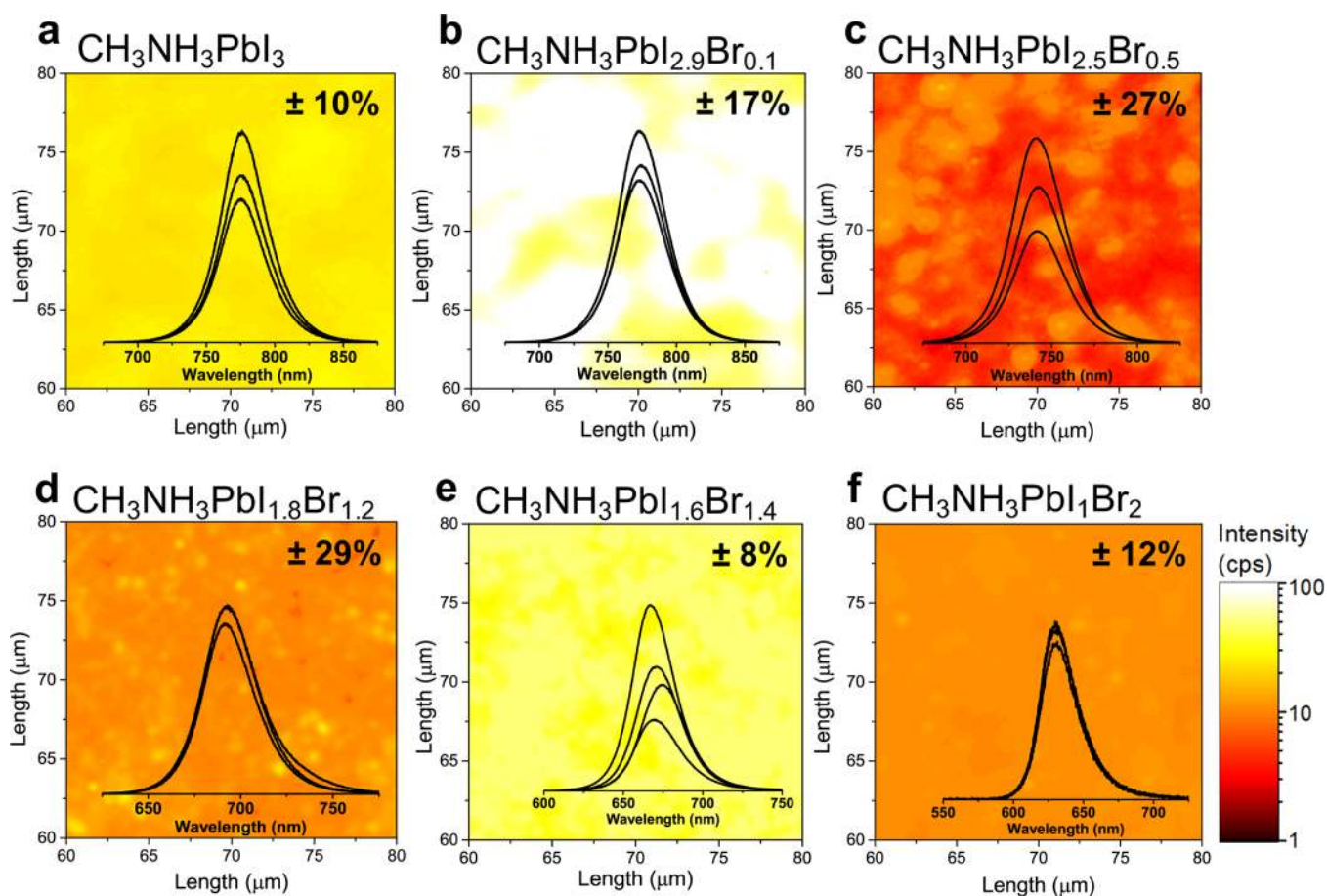
Figure 3. Photoluminescence imaging of Br-containing perovskite films. (a–f) Photoluminescence imaging in counts per second and the corresponding standard deviation (given in %) taken over an area $>100 \times 100\ \mu m^2$. The insets show representative variation of PL spectra from spot-to-spot.

recombination and, as a result, reduce the iQY. High QY, however, is important for solar cells because it directly affects the open-circuit voltage (V_{oc}) and thus the conversion efficiency.[29] The optically implied V_{oc} is defined as $qV_{oc} = E_g - T\Delta S - kT\ln QY$,[29,30] where q is the elementary charge, E_g is the band gap, k is the Boltzmann constant, T is the absolute temperature, and S is the entropy. The recombination as a function of optical carrier injection in these materials is studied by using pump-power-dependent photoluminescence measurements. The pump-power corresponds to an effective carrier concentration in the material, as generated by light, and is referred to as optical carrier injection. From these results we are able to predict an optimum carrier concentration for the respective material compositions at which the intrinsic optoelectronic quality is the highest as reflected by the maximum iQY.

Most of the studies on optoelectronic properties of perovskites have been centered around the pure $CH_3NH_3PbI_3$[9,11,23,31,32] and mixed $CH_3NH_3PbI_{3-x}Cl_x$[9,10,13,14,23,32,33] compositions. Only a few studies have reported on the optoelectronic properties beyond band gap and absorption coefficient of mixed I/Br lead halide perovskites.[7,34−37] While high iQY has been demonstrated only for the low band gap perovskites ($E_g \sim 1.6$ eV) without Br,[13,14] this study addresses the full band gap range and investigates the mixed lead halide perovskites ($CH_3NH_3PbI_{3-x}Br_x$), thereby significantly broadening the spectrum of possible applications

in optoelectronic devices. We present a synthetic approach to fabricate high optoelectronic quality $CH_3NH_3PbI_{3-x}Br_x$ over the entire composition range and demonstrate impressive iQY values up to 30% using in-depth photoluminescence-based characterization as a function of halide composition. Most notably, the iQY is high over the entire band gap range, which translates into high optically implied open-circuit voltage. Furthermore, halide perovskites synthesized using our approach exhibit significantly improved phase stability over an expanded composition range. This study thus establishes the potential of the band gap tunable $CH_3NH_3PbI_{3-x}Br_x$ (1.6 eV $\leq E_g \leq$ 2.3 eV) system as an efficient and low-cost building block for both solar cells and light-emitting devices.

Perovskite thin films with varying Br concentration were fabricated by a two-step low pressure vapor-assisted solution process (LP-VASP) that is adapted to previous reports[38,39] to allow controllable synthetic access to the full $CH_3NH_3PbI_{3-x}Br_x$ composition space, as depicted in Figure 1. First, mixed lead halide ($PbI_2/PbBr_2$) was spin-coated onto the glass substrate and dried at 110 °C for 15 min. Second, the precursor film was annealed in CH_3NH_3I/CH_3NH_3Br vapor at 120 °C for 2 h under a pressure of ~0.4 Torr.[39] Br incorporation occurs via a dynamic exchange with the vapor and the equilibrium composition is defined by the partial pressures of the CH_3NH_3I/CH_3NH_3Br precursors in the vapor phase (for more details, see Methods section in the Supporting Information). It is demonstrated that the full compositional
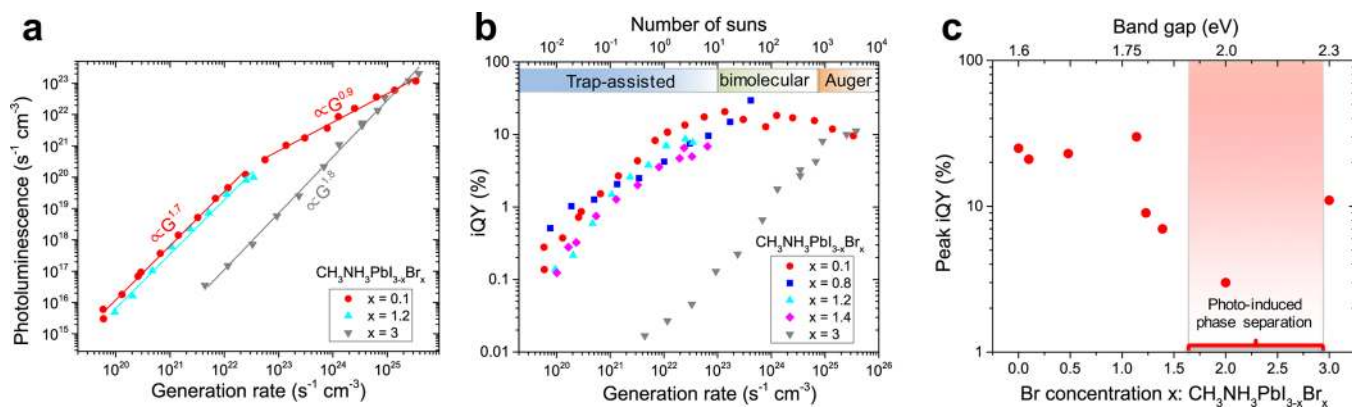
Figure 4. Steady-state photoluminescence. (a) Pump-power dependence of the integrated photoluminescence signal for three Br concentrations. (b) Pump-power dependence of the iQY. (c) Summary of iQY versus $CH_3NH_3PbI_{3-x}Br_x$ composition and corresponding band gap.

range of $CH_3NH_3PbI_{3-x}Br_x$ ($x = 0-3$) can be processed with very high spatial uniformity. Perovskite films were coated with a ~30 nm thick poly(methyl methacrylate) (PMMA) capping layer to prevent exposure to moisture, which is known to cause degradation in this material system.[40] Top view SEM images (Supporting Information, Figure S1) show that films are highly faceted, pinhole free and exhibit grain sizes mostly ~100 nm up to ~500 nm. Figure 2a shows the optical absorption spectra obtained from transmittance ($T\%$) and reflectance ($R\%$) measurements taken for the full range of band gap tuned perovskite films. All samples exhibit sharp absorption onsets above the band edge, with absorption coefficients $\alpha > 10^4$ cm^{-1} (Supporting Information, Figure S2a). An increase in the Br concentration monotonically shifts the absorption onset to higher energies. The nonlinear dependence of the band gap on composition x can be fitted with the empirical equation $E_g(x) = E_g(CH_3NH_3PbBr_3)(x/3) + E_g(CH_3NH_3PbI_3)(1 - (x/3)) - (x/3)(1 - (x/3))b$ with the bowing parameter $b = 0.34$ and $0 \leq x \leq 3$ is the atomic Br fraction (Supporting Information, Figure S2b). The obtained bowing parameter is in good agreement with literature.[7] Samples with composition $x \geq 2$ exhibit a peak at the absorption edge that is likely related to an excitonic transition that appears due to the higher exciton binding energy[41] at high Br concentration. The below band gap absorption artifact seen for all samples is caused by constructive thin-film interference effects due to multiple reflections at the air/PMMA and PMMA/perovskite interfaces. Steady-state PL spectra are presented in Figure 2b. The PL spectra are slightly blue shifted (anti-Stokes shift of ~10 nm or 30 meV) with respect to the absorption onset. The precise position of the absorption edge, as well as the PL peak position, can change depending on the exciton binding energy and self-absorption in the perovskite film[23] or as a result of the lattice phonon–photon interaction.

The X-ray diffraction (XRD) patterns (Figure 2c) of the perovskite films reveal that there is no phase separation into I- and Br-rich domains. These data also indicate that the majority of the starting $PbI_2/PbBr_2$ precursor is converted to the mixed halide $CH_3NH_3PbI_{3-x}Br_x$ phase by incorporation of Br via the gas phase (compare Figure 1). The (110) peak gradually shifts to larger angles with increasing Br concentration (XRD zoom in Figure 2d) due to the decreasing lattice parameter with increasing x.

The optoelectronic uniformity of the perovskite films was characterized via PL imaging over large areas (>100 × 100 μm^2) by analyzing the integrated luminescence peak. The PL

images as well as the standard deviation of the measured luminescence are presented in Figure 3. The spatial homogeneity exhibits a maximum standard deviation of <30%. The insets illustrate the point-to-point variation of the PL spectra with invariant lineshapes, confirming the uniformity of the films. While we note that local intra- and intergrain nonuniformities may exist at length scales below those probed here,[10] our results indicate excellent homogeneity over large areas and are consistent with the reproducible iQY measurements presented in this work (Supporting Information, Figure S8c).

Next, the pump-power-dependent steady-state PL at room temperature under ambient conditions (20–21 °C, 40–60% relative humidity) was investigated to identify the recombination regimes occurring in the perovskite films as a function of optically injected carrier concentration. Figure 4a illustrates the pump-power dependence of the PL intensity over a 6 orders of magnitude dynamic range with a minimum power of 7×10^{-4} W/cm^2 up to a maximum power of 5×10^2 W/cm^2. The excitation intensity is divided by the film thickness (which almost exactly matches complete absorption at the respective wavelength) to establish the generation rate G (s^{-1} cm^{-3}). The measurements were performed starting at the lowest pump-power and were terminated when sample degradation was observed as the pump-power was increased (for experimental details see Supporting Information). To extract reliable PL data that reflect the pure $CH_3NH_3PbI_{3-x}Br_x$ quality, samples were measured directly after fabrication and verification of the absence of PbI_2 that would lead to an increase of the PL signal, thus the iQY (Supporting Information Figure S3).

It is important to note that various illumination-induced effects were observed in the course of this work. Data points at the respective pump-power are only considered in this study if the spectral shape and position of the PL signal did not change during the measurement. By exceeding an illumination intensity threshold (that is specific to the Br concentration, Supporting Information Figure S4 and Figures S5c+d) a reversible shift in PL spectra by up to ~20 nm (or 45 meV) accompanied by a drop in intensity is observed (Supporting Information, Figure S5b). However, at very high illumination intensities (that are specific to the Br concentration and beyond the illumination intensities reported in Figure 4b) the samples degrade irreversibly (Supporting Information, Figure S6).

Samples with $x > 1.25$ (Supporting Information, Figure S4) are more prone to show a spectral red shift and slight peak broadening with increasing pump-power. At low pump-power,

the PL intensity is nearly constant over time, referring to the time window when samples were under constant illumination to extract the PL intensity (integration times of up to 120 s were used at low pump-power, Supporting Information, Figure S7a). Illumination-induced phase transformations of $CH_3NH_3PbI_{3-x}Br_x$ have been previously reported.[42] Films prepared by spin-coating of the precursor followed by hot plate annealing were previously shown to undergo light-induced reversible phase separation for $x \geq 0.6$ at 0.15 suns illumination intensity within less than a minute.[42] This was attributed to the formation of I-rich domains.[42] In comparison, for LP-VASP $CH_3NH_3PbI_{3-x}Br_x$ samples with $x = 1.4$ only a small spectral red shift is observed within 2 min at 2 suns illumination intensity (Supporting Information, Figure S7b). The observed red shift is small compared to the previous report and might be explained by minor illumination-induced local compositional variation in the Br/I ratio. A reversible phase segregation under illumination (below 1 sun), similar to the previous report of solution processed thin films,[42] was only seen for $x \geq 2$ (Supporting Information, Figure S7c). We conclude that the material quality and stability of $CH_3NH_3PbI_{3-x}Br_x$ grown from our LP-VASP exhibits improved light-stability over solution processed films.

The luminescence intensity versus generation rate G (Figure 4a and Supporting Information Figure S8a) is characterized by power law fits that indicate two regimes for the mixed halide samples. Up to a generation rate of $G \sim 3 \times 10^{22}$ s^{-1} cm^{-3} ($\sim$30 suns; 1-sun is used equivalent to the power density of 100 mW/cm^2) the curves follow a dependence $\propto G^{1.7}$, and for generation rates above 3×10^{22} s^{-1} cm^{-3} the luminescence intensity is $\propto G^{0.9}$. Power law dependences larger than one are indicative of SRH like recombination, that is intragap trap-assisted recombination instead of direct electron–hole recombination (bimolecular recombination). A PL intensity dependence with the generation rate $\propto G^{1.5}$ was observed by Saba et al.[23] At low intensities, traps are filled first, before bimolecular recombination starts to dominate as the pump-power increases. The pure Br sample ($x = 3$) exhibits a single trend line that is $\propto G^{1.8}$ indicating only monomolecular recombination over the investigated generation rate.

The QY is extracted from the pump-power-dependent PL measurements. The measured external luminescence efficiency is corrected for the band-edge refractive index[43] to determine the internal quantum yield (iQY). The details of the measurement setup and calibration of the PL data are reported in our previous study.[44] With increasing pump-power, the iQY rises for all samples, indicating that trap states lead to low iQY at low optical injection levels (see Figure 4b, Supporting Information Figure S8b). As seen in the pump-power-dependent luminescence study (Figure 4a), bimolecular recombination dominates when reaching $G \geq 3 \times 10^{22}$ s^{-1} cm^{-3} (slope $\propto$1), where the iQY is constant over almost 2 orders of magnitude of generation rate (observable for sample with $x = 0.1$). At higher optical injection, Auger recombination begins to dominate, leading to a drop in iQY when exceeding a generation rate $G \sim 5 \times 10^{24}$ s^{-1} cm^{-3} ($\sim$500 suns). Please note that the Auger regime reported here is not caused by sample degradation. The iQY of the pure Br sample ($x = 3$) shows a completely different behavior. First, the iQY in general is almost 2 orders of magnitude lower compared to mixed halide samples at the respective pump-power. Second, the iQY increases over the entire range of investigated generation rates, indicating a limitation by monomolecular trap assisted

recombination. Possibly, this could imply a higher trap density in the pure Br sample or different trap population/depopulation kinetics as compared to the mixed $CH_3NH_3PbI_{3-x}Br_x$ samples. As outlined above, the absorption spectrum of the pure Br sample clearly exhibits an excitonic feature that might limit charge carrier dynamics as well. The iQY of the investigated samples reaches a maximum value of 30%. We would like to highlight, that all $CH_3NH_3PbI_{3-x}Br_x$ samples over the full band gap range exhibit remarkably high iQY values, as summarized in Figure 4c (the upper x-axis as a function of the Br concentration is obtained by using the equation given in the Supporting Information, Figure S2b). It is noted that our reported iQY values for samples in which the Auger regime cannot be reached do not represent the maximum achievable values but are instead limited by material degradation under intense illumination (that strongly depends on the Br concentration). The spot-to-spot variation of the iQY on the same sample is minimal as shown in the Supporting Information, Figure S8c.

To elucidate the possible effect of laser illumination-induced heating of the perovskite thin films, PL is studied over a temperature range of 170−410 K (Supporting Information, Figure S9). The lower bound of the temperature-dependent measurements is set by a phase change from a tetragonal to an orthorhombic crystal system at 150 K[45,46] and the higher bound is limited by the PMMA glass transition temperature. Surprisingly, the sample shows extraordinary stability at elevated temperatures with a PL intensity drop to 65% of the room temperature value at 400 K. With decreasing temperature, we see a small red shift in the PL spectra. This finding was observed earlier for $CH_3NH_3PbI_3$ as well as $CH_3NH_3PbI_{3-x}Cl_x$ and is often seen for Pb-containing semiconductors.[46] Moreover, the PL intensity increases by 40% at 210 K, relative to the room-temperature value (Supporting Information, Figure S9). A 40% PL intensity increase directly translates to the same increase in the iQY. The rise of iQY with decreasing temperature can simply be explained by a reduced trap activity, which eventually diminishes to zero at sufficiently low temperatures. An increase in iQY with decreasing temperature was found for $CH_3NH_3PbI_{3-x}Cl_x$ as well.[14]

Pulsed laser excitation of $CH_3NH_3PbI_{3-x}Br_x$ samples was investigated to extract the minority carrier lifetimes. Results are discussed in the Supporting Information, along with the modeling of both the TRPL and steady-state iQY data (Figures S10 and 11).

In order to relate the above presented results to the V_{oc}, an important metric for solar cells, the optically implied V_{oc} is calculated and illustrated in Figure 5. Here, the optically implied V_{oc} reflects the maximum V_{oc} that can be achieved purely based on the intrinsic material quality, assuming no optical losses nor losses caused by nonideal contact architectures. Thus, the implied V_{oc} is calculated here via $qV_{oc} = E_g − T\Delta S − kT|\ln iQY|$ using the iQY instead of the external QY.[29,30] That is, the V_{oc} (i.e., chemical potential difference) is treated as a thermodynamic variable, where the entropy due to nonideality is equal to 260 meV in the band gap range of 1.0−1.8 eV.[47−49] Figure 5 illustrates the evolution of the optically implied V_{oc} with increasing band gap at 1 sun (blue squares) as well as under optimized carrier injection level (red circles) as calculated from the maximum iQY. The V_{oc} deficit ($E_g/q − V_{oc}$) is about 400 mV at 1 sun up to a band gap of 1.97 eV and increases to 480 mV at 2.28 eV. The V_{oc} deficit can be reduced
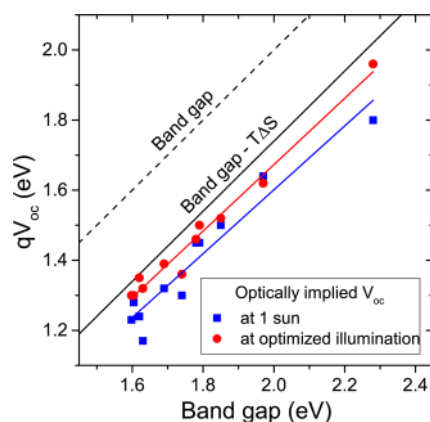
Figure 5. Optically implied V_{oc} ($qV_{oc} = E_g - T\Delta S - kT|\ln iQY|$), representing the V_{oc} that can be obtained based on the intrinsic material quality as a function of band gap, at one sun equivalent (blue squares) and at optimized illumination (red points). Optimized illumination refers to the carrier injection level at which the iQY is at the maximum value. Blue and red solid lines show linear fits to the data. Dashed line, band gap; solid line, band gap less $T\Delta S$.

by ~60 mV for samples with Br concentration up to $x = 2$ and by 150 mV for the pure Br sample at the respective optimized carrier injection level (i.e., illumination intensity) for each composition. Please note that the optimized carrier injection is extracted from the iQY versus pump-power analysis. Samples with $x > 0.8$ show 1 sun V_{oc} very close to the optimized carrier injection conditions because the samples degrade under higher pump-powers thus higher generation rates cannot be accessed experimentally in this study. The best state-of-the art perovskite solar cells with band gaps of ~1.55 eV, exhibit electrical V_{oc} deficits of about 450 mV.[50] As a comparison, the lowest reported V_{oc} deficit is 298 mV, which has been achieved in high quality single crystalline GaAs solar cells.[16] In literature on perovskite solar cell devices, the electrical V_{oc} values drop significantly with increasing band gap (see Supporting Information, Figure S12). This study points out that the reported electrical V_{oc} of higher band gap perovskites is limited by the choice of the selective contact material but not the perovskite material itself if Br-containing films using the described process are utilized. It is noted that for solar cell applications, it is desirable to optimize the perovskite film in such a way that the highest iQY can be obtained at 1 sun. One possibility in this regard is to chemically dope the films, similar to what is often performed in classical inorganic semiconductors. It was reported, for example, that by appropriately choosing the growth condition, such as using a chlorine-rich as opposed to an iodine-rich precursor, the trap density can be lowered.[51]

In summary, we have established a low-pressure vapor-assisted solution process that is adapted to synthetically access the full set of band gap tunable $CH_3NH_3PbI_{3-x}Br_x$ perovskites with phase purity. Uniform and high quality films were obtained and studied by photoluminescence based spectroscopy over the full compositional range of $x = 0-3$. The dependency of iQY on generation rate (i.e., illumination intensity), which defines the optically injected carrier concentration, was used to determine the optimal operation range for each perovskite composition. Our results indicate that Br-containing perovskites exhibit high optoelectronic quality over the entire compositional range (1.6 eV $\leq E_g \leq$ 2.3 eV) with iQYs as high as 30%. Importantly, we observe improved

photostability of $CH_3NH_3PbI_{3-x}Br_x$ films formed by LP-VASP compared to previously reported solution-processed material. Though the samples exhibit better photostability, this still represents a limitation for the use of mixed I/Br halide perovskites in solar cells and has to be addressed by further process engineering. On the basis of this study, we conclude that hybrid organic−inorganic mixed halide perovskites $CH_3NH_3PbI_{3-x}Br_x$ possess suitable optical band gaps and high iQY, which makes them highly promising candidates as top cell materials in conjunction with industry dominated Si bottom cells. Future work should focus on building perovskite/Si tandem photovoltaic cells using the described Br-containing films.

■ ASSOCIATED CONTENT

ⓢ Supporting Information

The Supporting Information is available free of charge on the ACS Publications website at DOI: 10.1021/acs.nano-lett.5b04884.

(Detailed experimental procedures, Figures S1−12, and kinetic modeling of PL and TRPL data. PDF)

■ AUTHOR INFORMATION

Corresponding Authors
*E-mail (I.D.S.): idsharp@lbl.gov.
*E-mail (A.J.): ajavey@berkeley.edu.

Author Contributions
The manuscript was written through contributions of all authors. All authors have given approval to the final version of the manuscript.

C.M.S.-F. and Y.L. contributed equally.

Notes
The authors declare no competing financial interest.

■ REFERENCES

(1) Stranks, S. D.; Snaith, H. J. *Nat. Nanotechnol.* **2015**, *10*, 391−402.
(2) Nie, W.; Tsai, H.; Asadpour, R.; Blancon, J.-C.; Neukirch, A. J.; Gupta, G.; Crochet, J. J.; Chhowalla, M.; Tretiak, S.; Alam, M. A.; Wang, H.-L.; Mohite, A. D. *Science* **2015**, *347*, 522−525.
(3) Docampo, P.; Hanusch, F. C.; Stranks, S. D.; Döblinger, M.; Feckl, J. M.; Ehrensperger, M.; Minar, N. K.; Johnston, M. B.; Snaith, H. J.; Bein, T. *Adv. Energy Mater.* **2014**, *4*, 1400355.
(4) Ball, J. M.; Lee, M. M.; Hey, A.; Snaith, H. J. *Energy Environ. Sci.* **2013**, *6*, 1739−1743.

(5) Yin, W.-J.; Shi, T.; Yan, Y. *Appl. Phys. Lett.* **2014**, *104*, 0639031−0639034.

(6) Kim, J.; Lee, S.-H.; Lee, J. H.; Hong, K.-H. *J. Phys. Chem. Lett.* **2014**, *5*, 1312−1317.

(7) Noh, J. H.; Im, S. H.; Heo, J. H.; Mandal, T. N.; Seok, S. I. *Nano Lett.* **2013**, *13*, 1764−1769.

(8) De Wolf, S.; Holovsky, J.; Moon, S.-J.; Löper, P.; Niesen, B.; Ledinsky, M.; Haug, F.-J.; Yum, J.-H.; Ballif, C. *J. Phys. Chem. Lett.* **2014**, *5*, 1035−1039.

(9) Stranks, S. D.; Eperon, G. E.; Grancini, G.; Menelaou, C.; Alcocer, M. J. P.; Leijtens, T.; Herz, L. M.; Petrozza, A.; Snaith, H. J. *Science* **2013**, *342*, 341−344.

(10) de Quilettes, D. W.; Vorpahl, S. M.; Stranks, S. D.; Nagaoka, H.; Eperon, G. E.; Ziffer, M. E.; Snaith, H. J.; Ginger, D. S. *Science* **2015**, *348*, 683−686.

(11) Xing, G.; Mathews, N.; Sun, S.; Lim, S. S.; Lam, Y. M.; Grätzel, M.; Mhaisalkar, S.; Sum, T. C. *Science* **2013**, *342*, 344−347.

(12) Dong, Q.; Fang, Y.; Shao, Y.; Mulligan, P.; Qiu, J.; Cao, L.; Huang, J. *Science* **2015**, *347*, 967−970.

(13) Deschler, F.; Price, M.; Pathak, S.; Klintberg, L. E.; Jarausch, D.-D.; Higler, R.; Hüttner, S.; Leijtens, T.; Stranks, S. D.; Snaith, H. J.; Atatüre, M.; Phillips, R. T.; Friend, R. H. *J. Phys. Chem. Lett.* **2014**, *5*, 1421−1426.

(14) Stranks, S. D.; Burlakov, V. M.; Leijtens, T.; Ball, J. M.; Goriely, A.; Snaith, H. J. *Phys. Rev. Appl.* **2014**, *2*, 034007.

(15) Jeon, N. J.; Noh, J. H.; Yang, W. S.; Kim, Y. C.; Ryu, S.; Seo, J.; Seok, S. I. *Nature* **2015**, *517*, 476−480.

(16) Green, M. A.; Emery, K.; Hishikawa, Y.; Warta, W.; Dunlop, E. D. *Prog. Photovoltaics* **2015**, *23*, 1−9.

(17) Löper, P.; Moon, S.-J.; de Nicolas, S. M.; Niesen, B.; Ledinsky, M.; Nicolay, S.; Bailat, J.; Yum, J.-H.; Wolf, S. D.; Ballif, C. *Phys. Chem. Chem. Phys.* **2014**, *17*, 1619−1629.

(18) Mailoa, J. P.; Bailie, C. D.; Johlin, E. C.; Hoke, E. T.; Akey, A. J.; Nguyen, W. H.; McGehee, M. D.; Buonassisi, T. *Appl. Phys. Lett.* **2015**, *106*, 121105.

(19) Bailie, C. D.; Christoforo, M. G.; Mailoa, J. P.; Bowring, A. R.; Unger, E. L.; Nguyen, W. H.; Burschka, J.; Pellet, N.; Lee, J. Z.; Grätzel, M.; Noufi, R.; Buonassisi, T.; Salleo, A.; McGehee, M. D. *Energy Environ. Sci.* **2015**, *8*, 956−963.

(20) Kranz, L.; Abate, A.; Feurer, T.; Fu, F.; Avancini, E.; Löckinger, J.; Reinhard, P.; Zakeeruddin, S. M.; Grätzel, M.; Buecheler, S.; Tiwari, A. N. *J. Phys. Chem. Lett.* **2015**, *6*, 2676−2681.

(21) Tan, Z.-K.; Moghaddam, R. S.; Lai, M. L.; Docampo, P.; Higler, R.; Deschler, F.; Price, M.; Sadhanala, A.; Pazos, L. M.; Credgington, D.; Hanusch, F.; Bein, T.; Snaith, H. J.; Friend, R. H. *Nat. Nanotechnol.* **2014**, *9*, 687−692.

(22) Ning, Z.; Gong, X.; Comin, R.; Walters, G.; Fan, F.; Voznyy, O.; Yassitepe, E.; Buin, A.; Hoogland, S.; Sargent, E. H. *Nature* **2015**, *523*, 324−328.

(23) Saba, M.; Cadelano, M.; Marongiu, D.; Chen, F.; Sarritzu, V.; Sestu, N.; Figus, C.; Aresti, M.; Piras, R.; Geddo Lehmann, A.; Cannas, C.; Musinu, A.; Quochi, F.; Mura, A.; Bongiovanni, G. *Nat. Commun.* **2014**, *5*, 5049.

(24) Bremner, S. P.; Levy, M. Y.; Honsberg, C. B. *Prog. Photovoltaics* **2008**, *16*, 225−233.

(25) Essig, S.; Ward, S.; Steiner, M. A.; Friedman, D. J.; Geisz, J. F.; Stradins, P.; Young, D. L. *Energy Procedia* **2015**, *77*, 464−469.

(26) Soga, T.; Baskar, K.; Kato, T.; Jimbo, T.; Umeno, M. *J. Cryst. Growth* **1997**, *174*, 579−584.

(27) Hsu, L.; Walukiewicz, W. *J. Appl. Phys.* **2008**, *104*, 024507.

(28) Reichertz, L. A.; Gherasoiu, I.; Yu, K. M.; Kao, V. M.; Walukiewicz, W.; Ager, J. W., III *Appl. Phys. Express* **2009**, *2*, 122202.

(29) Miller, O. D.; Yablonovitch, E.; Kurtz, S. R. *IEEE J. Photovolt.* **2012**, *2*, 303−311.

(30) Ross, R. T. *J. Chem. Phys.* **1967**, *46*, 4590−4593.

(31) La-o-vorakiat, C.; Salim, T.; Kadro, J.; Khuc, M.-T.; Haselsberger, R.; Cheng, L.; Xia, H.; Gurzadyan, G. G.; Su, H.; Lam, Y. M.; Marcus, R. A.; Michel-Beyerle, M.-E.; Chia, E. E. M. *Nat. Commun.* **2015**, *6*, 7903.

(32) D'Innocenzo, V.; Srimath Kandada, A. R.; De Bastiani, M.; Gandini, M.; Petrozza, A. *J. Am. Chem. Soc.* **2014**, *136*, 17730−17733.

(33) Chen, Q.; Zhou, H.; Fang, Y.; Stieg, A. Z.; Song, T.-B.; Wang, H.-H.; Xu, X.; Liu, Y.; Lu, S.; You, J.; Sun, P.; McKay, J.; Goorsky, M. S.; Yang, Y. *Nat. Commun.* **2015**, *6*, 7269.

(34) Liang, P.-W.; Chueh, C.-C.; Xin, X.-K.; Zuo, F.; Williams, S. T.; Liao, C.-Y.; Jen, A. K.-Y. *Adv. Energy Mater.* **2015**, *5*, 1400960.

(35) Eperon, G. E.; Stranks, S. D.; Menelaou, C.; Johnston, M. B.; Herz, L. M.; Snaith, H. J. *Energy Environ. Sci.* **2014**, *7*, 982−988.

(36) Yang, Y.; Yan, Y.; Yang, M.; Choi, S.; Zhu, K.; Luther, J. M.; Beard, M. C. *Nat. Commun.* **2015**, *6*, 7961.

(37) Park, B.; Philippe, B.; Jain, S. M.; Zhang, X.; Edvinsson, T.; Rensmo, H.; Zietz, B.; Boschloo, G. *J. Mater. Chem. A* **2015**, *3*, 21760−21771.

(38) Chen, Q.; Zhou, H.; Hong, Z.; Luo, S.; Duan, H.-S.; Wang, H.-H.; Liu, Y.; Li, G.; Yang, Y. *J. Am. Chem. Soc.* **2014**, *136*, 622−625.

(39) Li, Y.; Cooper, J. K.; Buonsanti, R.; Giannini, C.; Liu, Y.; Toma, F. M.; Sharp, I. D. *J. Phys. Chem. Lett.* **2015**, *6*, 493−499.

(40) Matsumoto, F.; Vorpahl, S. M.; Banks, J. Q.; Sengupta, E.; Ginger, D. S. *J. Phys. Chem. C* **2015**, *119*, 20810−20816.

(41) Tanaka, K.; Takahashi, T.; Ban, T.; Kondo, T.; Uchida, K.; Miura, N. *Solid State Commun.* **2003**, *127*, 619−623.

(42) Hoke, E. T.; Slotcavage, D. J.; Dohner, E. R.; Bowring, A. R.; Karunadasa, H. I.; McGehee, M. D. *Chem. Sci.* **2015**, *6*, 613−617.

(43) Yablonovitch, E.; Cody, G. D. *IEEE Trans. Electron Devices* **1982**, *29*, 300−305.

(44) Amani, M.; Lien, D.-H.; Kiriya, D.; Xiao, J.; Azcatl, A.; Noh, J.; Madhvapathy, S. R.; Addou, R.; Kc, S.; Dubey, M.; Cho, K.; Wallace, R. M.; Lee, S.-C.; He, J.-H.; Ager, J. W.; Zhang, X.; Yablonovitch, E.; Javey, A. *Science* **2015**, *350*, 1065−1068.

(45) Mashiyama, H.; Kurihara, Y.; Azetsu, T. *J. Korean Phys. Soc.* **1998**, *32*, 156−158.

(46) D'Innocenzo, V.; Grancini, G.; Alcocer, M. J. P.; Kandada, A. R. S.; Stranks, S. D.; Lee, M. M.; Lanzani, G.; Snaith, H. J.; Petrozza, A. *Nat. Commun.* **2014**, *5*, 3586.

(47) Markvart, T. *Phys. Status Solidi A* **2008**, *205*, 2752−2756.

(48) Hirst, L. C.; Ekins-Daukes, N. J. *Prog. Photovoltaics* **2011**, *19*, 286−293.

(49) Miller, O. D. *Photonic Design: From Fundamental Solar Cell Physics to Computational Inverse Design*; University of California: Berkeley, 2012.

(50) Snaith, H. J. *J. Phys. Chem. Lett.* **2013**, *4*, 3623−3630.

(51) Buin, A.; Pietsch, P.; Xu, J.; Voznyy, O.; Ip, A. H.; Comin, R.; Sargent, E. H. *Nano Lett.* **2014**, *14*, 6281−6286.